

Model-Dependent Prosthesis Control with Real-Time Force Sensing

Rachel Gehlhar, Je-han Yang, and Aaron D. Ames

Abstract—Lower-limb prosthesis wearers are more prone to fall than non-amputees. Powered prosthesis can reduce this instability of passive prostheses. While shown to be more stable in practice, powered prostheses generally use model-independent control methods that lack formal guarantees of stability and rely on heuristic tuning. Recent work overcame one of the limitations of model-based prosthesis control by developing a class of stable prosthesis subsystem controllers independent of the human model, except for its interaction forces with the prosthesis. Force sensors to measure these socket interaction forces as well as the ground reaction forces (GRFs) could introduce noise into the control loop making hardware implementation infeasible. This paper addresses part of this limitation by obtaining some of the GRFs through an insole pressure sensor. This paper achieves the first model-dependent prosthesis controller that uses in-the-loop on-board real-time force sensing, resulting in stable human-prosthesis walking and increasing the validity of our formal guarantees of stability.

I. INTRODUCTION

Lower-limb prosthesis users fall more frequently than non-amputees [1]. A survey in [2] found 45% of polled amputees had fallen in the past year while wearing their prosthesis. This instability could be due to their passive prostheses, which can be less stable than powered prostheses [3]. Current powered prosthesis control methods tend to be model-independent [4], [5], requiring heuristic tuning, lacking formal guarantees of stability, and not utilizing the system’s natural dynamics. Lower-limb prosthesis users’ gait stability can be assessed through plantar pressure data [6]. Utilizing this data in control could improve stability. This motivates developing model-dependent prosthesis control methods with accurate GRF knowledge to guarantee stability.

A challenge arises in developing model-dependent prosthesis controllers: the human dynamics are unknown. The work of [7] addressed this limitation by developing rapidly exponentially stabilizing control Lyapunov functions (RES-CLFs), which were shown to stabilize bipedal robotic walking [8], in the context of separable systems [9]. This resulted in a class of stabilizing prosthesis controllers relying only on local prosthesis information. Previously, RES-CLFs were difficult to realize on hardware due to the typical required inversion of the inertia matrix which is computationally expensive and susceptible to error. The work of [10] developed and demonstrated a RES-CLF controller on a bipedal robot

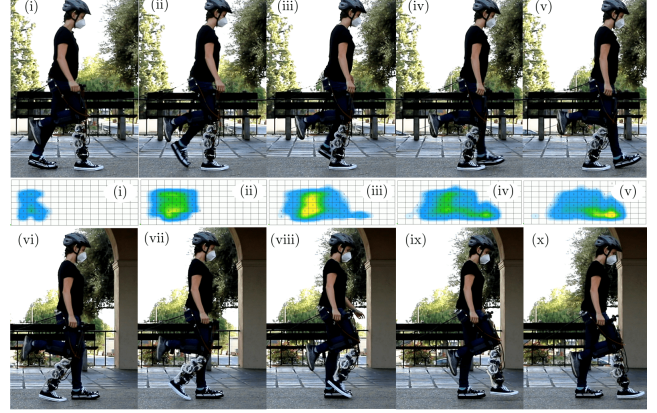


Fig. 1. Gait tiles of human subject walking with model-dependent prosthesis controller using real-time pressure measurements. The numerals correspond to phases of the gait in the trajectory of Fig. 5. (Top) Prosthesis stance phase. (Middle) Pressure map readings corresponding to the phase of the gait cycle. (Bottom) Prosthesis in non-stance phase.

without inverting the inertia matrix by constructing the RES-CLF in an inverse dynamics framework in a quadratic program (QP). The work of [10] brings the class of controllers developed in [7] closer to being implementable.

Realizing RES-CLF controllers on prostheses meets an additional challenge: they require knowledge of both the ground reaction forces and moment and socket interaction forces and moment. (For simplicity we refer to these as “GRFs” and “socket forces”.) Measuring these forces typically requires load cells in the prosthesis platform and the noise of these sensors could corrupt the control input signal. The work of [11] realized the first model-dependent prosthesis controller with consideration for the forces, using holonomic constraints for the GRFs and force estimation for the socket forces. However using holonomic constraints to determine GRFs assumes a rigid contact with the ground, inaccurately representing many real-life scenarios where the terrain deforms under a load, like granular media [12]. Developing control methods accounting for non-rigid terrain is especially important for prostheses to enable amputees to walk stably on a variety of surfaces present in daily life.

Powered prostheses with load cells at their ankles can detect GRFs and center of pressure (CoP) [5], [13], [14]. The work of [13], used GRF sensing capability to determine motion intent to trigger transitions between gait phases of finite-state based impedance control. The work of [5] used the CoP to encode and modulate virtual constraints for prosthesis control. To date, GRF measurements have not been included in the dynamics to achieve model-dependent prosthesis control. We desire a way to measure GRFs to provide accurate dynamics to our model-based controller as well as have CoP detection capabilities for future research to

*This material is based upon work supported by the National Science Foundation Graduate Research Fellowship under Grant No. DGE-1745301. This research was approved by California Institute of Technology Institutional Review Board with protocol no. 16-0693 for human subject testing.

R. Gehlhar and A. Ames are with the Department of Mechanical and Civil Engineering, J. Yang is with the Department of Electrical Engineering, California Institute of Technology, Pasadena, CA 91125 USA. Emails: {rgehlhar, ames, jyang5}@caltech.edu

assess gait health and symmetry [6], [15]. We seek a method without inclusion of a load cell, which requires prosthesis platform modifications, could add height to the platform, and may introduce noise into the controller. With an insole pressure sensor on a transfemoral powered prosthesis, this work implements the first model-dependent prosthesis controller that uses real-time force sensing to complete the dynamics, resulting in stable human-prosthesis walking.

In this paper, Section II overviews separable system control methods and RES-CLFs. Section III constructs the controller of focus in this work that utilizes the GRF measurements from an insole pressure sensor. Following, Section IV defines the amputee-prosthesis model and describes the gait generation method. Section V presents the selection criteria, hardware specifications, and software implementation details of the pressure sensor used in this study. This pressure sensor is integrated into the powered transfemoral prosthesis platform, AMPRO3, which is described in Section VI followed by the experimental set-up. Finally, the experimental results show the improved accuracy of our GRF model while achieving comparable tracking results to the controller calculating GRFs via holonomic constraints. The main contributions of this paper are

- integrating an insole pressure sensor into a powered prosthesis platform for real-time GRF sensing and to enable future gait analysis and CoP control methods,
- achieving stable human-prosthesis walking through model-dependent prosthesis control with in-the-loop on-board real-time force sensing, and
- improving our prosthesis contact model accuracy to increase the validity of our formal guarantees of stability.

II. BACKGROUND ON SEPARABLE SUBSYSTEMS

To construct the controller used as the focus of this work and justify our claim of formal guarantees of stability for the whole human-prosthesis system, we will provide a brief overview of the separable subsystem framework along with RES-CLFs starting in the context of robotic control systems.

Robotic Control System. Consider a robotic control system in 2D space with η DOFs and configuration coordinates $q = (q_l^T, q_f^T, q_s^T)^T \in \mathbb{R}^\eta$ defining the configuration space \mathcal{Q} . We will focus on a subsystem of the robot defined by coordinates $q_s \in \mathbb{R}^{n_s}$ with m_s actuators. The remaining system is defined by $q_l \in \mathbb{R}^{n_l}$ with m_r actuators. The attachment point between these systems is modeled as a 3-DOF rigid joint (x, z Cartesian position, and pitch) and defined with coordinates q_f . Here $n_l + n_s + 3 = \eta$ and $m_s + m_r = m$, the total number of actuators. The coordinates q_l include the floating base coordinates $q_B \in \mathbb{R}^3$. The constrained dynamics of the full system are given by the following Euler-Lagrange equation [16]:

$$D(q)\ddot{q} + H(q, \dot{q}) = Bu + J_h^T(q)\lambda_h \quad (1)$$

$$J_h(q)\ddot{q} + \dot{J}_h(q, \dot{q})\dot{q} = 0, \quad (2)$$

where $D(q)$ is the inertia matrix, $H(q, \dot{q})$ is a vector containing Coriolis, centrifugal, and gravity forces, B is the

actuation matrix for $u \in \mathbb{R}^m$ control inputs, and $J_h(q)$ is the Jacobian of the holonomic constraints $h(q)$ and projects the constraint wrenches λ_h .

Robotic Subsystem. To develop model-based prosthesis subsystem controllers, we model the robotic *subsystem* separately with floating base coordinates $\bar{q}_B \in \mathbb{R}^3$ where it attaches to the remaining system. With subsystem configuration coordinates $\bar{q} = (\bar{q}_B^T, q_s^T)^T \in \mathbb{R}^{\bar{\eta}}$, where $\bar{\eta} = \eta_s + 3$, the constrained robotic subsystem dynamics are:

$$\bar{D}(\bar{q})\ddot{\bar{q}} + \bar{H}(\bar{q}, \dot{\bar{q}}) = \bar{B}u_s + \bar{J}_h^T(\bar{q})\bar{\lambda}_h + \bar{J}_f^T(\bar{q})F_f \quad (3)$$

$$\bar{J}_h(\bar{q})\ddot{\bar{q}} + \dot{\bar{J}}_h(\bar{q}, \dot{\bar{q}})\dot{\bar{q}} = 0. \quad (4)$$

Here F_f are the fixed joint interaction forces inputted to this system and projected into the dynamics by $\bar{J}_f(q)$. $\bar{J}_h(\bar{q})$ is the Jacobian of the $\bar{\eta}_h$ subsystem holonomic constraints $\bar{h}(\bar{q})$ with constraint wrench $\bar{\lambda}_h$. By solving for $\ddot{\bar{q}}$ in the dynamics (3) and substituting this into the holonomic constraint equation (4), we solve for the constraint wrenches:

$$\bar{\lambda}_h = (\bar{J}_h \bar{D}^{-1} \bar{J}_h^T)^{-1} (\bar{J}_h \bar{D}^{-1} (\bar{H} - \bar{B}u_s - \bar{J}_f^T F_f) - \dot{\bar{J}}_h \dot{\bar{q}}). \quad (5)$$

For the prosthesis, the work of [11] used (5) to calculate the GRFs modeled as holonomic constraints with the ground. For this paper we use the holonomic constraints to calculate the x-direction GRF but use a pressure sensor to measure the other GRFs: z-direction force and y-direction moment.

Separable Subsystems. With states $x_q = (q^T, \dot{q}^T)^T$, we write the full robotic system dynamics (1) as an ODE:

$$\dot{x}_q = \underbrace{\begin{bmatrix} \dot{q} \\ D^{-1}(q)(-H(q, \dot{q}) + J_h(q)^T \lambda_h) \end{bmatrix}}_{f_q(x_q)} + \underbrace{\begin{bmatrix} 0 \\ D^{-1}(q)(B) \end{bmatrix}}_{g_q(x_q)} u.$$

To apply the *separable system* framework of [9], we rearrange the states and define $x_r = (q_l^T, q_f^T, \dot{q}_l^T, \dot{q}_f^T)^T$ and $x_s = (q_s^T, \dot{q}_s^T)^T$ which, due to the fixed joint as explained in [9], yields a system of the following form:

$$\begin{bmatrix} \dot{x}_r \\ \dot{x}_s \end{bmatrix} = \underbrace{\begin{bmatrix} f^r(x) \\ f^s(x) \end{bmatrix}}_{f(x)} + \underbrace{\begin{bmatrix} g_1^r(x) & g_2^r(x) \\ 0 & g^s(x) \end{bmatrix}}_{g(x)} \begin{bmatrix} u_r \\ u_s \end{bmatrix}, \quad (6)$$

$$x_r \in \mathbb{R}^{n_r}, \quad x_s \in \mathbb{R}^{n_s}, \quad u_r \in \mathbb{R}^{m_r}, \quad u_s \in \mathbb{R}^{m_s}.$$

The remaining control input u_r does not affect the dynamics of x_s , allowing subsystem controller design with the x_s dynamics independent of the x_r dynamics. We define a *separable subsystem* and *remaining system* [7], [9], respectively,

$$\dot{x}_s = f^s(x) + g^s(x)u_s, \quad (7)$$

$$\dot{x}_r = f^r(x) + g_1^r(x)u_r + g_2^r(x)u_s. \quad (8)$$

Equivalent Subsystem. The subsystem dynamics still depend on the full system states so we alternatively express the dynamics of x_s as an ODE using (3) with a method similar to that used for the full-order dynamics:

$$\dot{x}_s = \bar{f}^s(\mathcal{X}) + \bar{g}^s(\mathcal{X})u_s, \quad (9)$$

$$\mathcal{X} = (\bar{x}_r^T, x_s^T, \zeta^T)^T \in \mathbb{R}^{\bar{n}}.$$

Here $\bar{x}_s = x_s$, $\bar{x}_r = (\bar{q}_B^T, \dot{\bar{q}}_B^T)^T \in \mathbb{R}^{\bar{n}_r}$ are *measurable states*, and \mathcal{X} is the vector of states $\bar{x} = (\bar{x}_r^T, x_s^T)^T$ and *measurable input* $\zeta = F_f \in \mathbb{R}^{n_f}$. This system equates to (7) by a transformation $T(x) = \mathcal{X}$, where $\bar{f}^s(\mathcal{X}) = f(x)$ and $\bar{g}^s(\mathcal{X}) = g^s(x)$ for all x . For this robotic system form, this transformation exists and is given in [9]. An IMU and force sensor could give \bar{x}_r and ζ in practice.

Separable Subsystem RES-CLF. With the subsystem now defined in locally available coordinates \mathcal{X} , we define a class of stabilizing model-dependent subsystem controllers. Using the work of [7] we construct a RES-CLF $\bar{V}_\varepsilon^s(x_s)$ for the equivalent subsystem,

$$\bar{c}_1^s \|x_s\|^2 \leq \bar{V}_\varepsilon^s(x_s) \leq \frac{\bar{c}_2^s}{\varepsilon} \|x_s\|^2 \quad (10)$$

$$\inf_{u_s \in \mathbb{R}^{m_s}} [\dot{\bar{V}}_\varepsilon^s(\mathcal{X}, u_s)] \leq -\frac{\bar{c}_3^s}{\varepsilon} \bar{V}_\varepsilon^s(x_s),$$

for all $0 < \varepsilon < 1$ and $\mathcal{X} \in \mathbb{R}^{\bar{n}}$, with constants $\bar{c}_1^s, \bar{c}_2^s, \bar{c}_3^s > 0$. All controllers that satisfy $\dot{\bar{V}}_\varepsilon^s(\mathcal{X}, u_s) \leq -\frac{\bar{c}_3^s}{\varepsilon} \bar{V}_\varepsilon^s(x_s)$ belong to the class $\bar{K}_\varepsilon^s(\mathcal{X})$:

$$\bar{K}_\varepsilon^s(\mathcal{X}) = \{u_s \in \mathbb{R}^{m_s} : \dot{\bar{V}}_\varepsilon^s(\mathcal{X}, u_s) \leq -\frac{\bar{c}_3^s}{\varepsilon} \bar{V}_\varepsilon^s(x_s)\}. \quad (11)$$

The work of [8] developed RES-CLF controllers with ε to tune ε to yield fast enough convergence such that a hybrid system and its zero dynamics would not be destabilized by the impact dynamics of the hybrid system.

Main Theoretic Idea. By the work of [7], when a RES-CLF stabilizes the remaining system (8), any controller $u_s \in \bar{K}_\varepsilon^s(\mathcal{X})$ stabilizes the full-order hybrid system with zero dynamics. Hence, separating a robotic system and constructing an equivalent subsystem provides a means to construct model-dependent subsystem controllers using solely local information guaranteeing full-order system stability while also utilizing the natural dynamics. In the case of a human-prosthesis system, we assume the human stabilizes itself based on research of central pattern generators which suggests biological walkers demonstrate stable rhythmic behavior [17], meaning they have limit cycles. All stabilizing controllers for these hybrid limit cycles belong to the class of RES-CLFs in [7] for the remaining system.

III. CONTROL METHODS

The ID-CLF-QP of [10] provides an implementable form of a RES-CLF. We outline this construction for an equivalent robotic subsystem (3) with the additional $\bar{J}_f^T(\bar{q})F_f$ term in the dynamics. We explain how we estimate this term and measure the GRFs for the prosthesis dynamics.

A. Controller Formulation

To develop a Lyapunov function for the ID-CLF-QP of [10] we construct outputs to feedback linearize the system and dictate the motion of the robot.

CLF Construction. We define linearly independent subsystem positional outputs to enforce desired trajectories on the robotic subsystem,

$$y_s(x_s) = y_s^a(x_s) - y_s^d(\tau(x_s), \alpha), \quad (12)$$

where $y_s^a(x_s)$ are the actual joint outputs and $y_s^d(\tau(x_s), \alpha)$ are the desired trajectories defined by parameters α and modulated by $\tau(x_s)$, a state-based phase variable. Taking the derivatives along the equivalent subsystem dynamics (9), we relate the outputs to the control input u_s :

$$\ddot{y}_s = L_{\bar{f}^s}^2 y_s(\mathcal{X}) + L_{\bar{g}^s} L_{\bar{f}^s} y_s(\mathcal{X}) u_s.$$

Here $L_{\bar{f}^s}^2 y_s(\mathcal{X})$ and $L_{\bar{g}^s} L_{\bar{f}^s} y_s(\mathcal{X})$ denote the Lie derivatives [18]. Because the outputs are linearly independent, $L_{\bar{g}^s} L_{\bar{f}^s} y_s(\mathcal{X})$ is invertible, making our system feedback linearizable [18] with feedback linearizing controller,

$$u_s(\mathcal{X}) = (L_{\bar{g}^s} L_{\bar{f}^s} y_s(\mathcal{X}))^{-1} (-L_{\bar{f}^s}^2 y_s(\mathcal{X}) + \nu), \quad (13)$$

with auxiliary control input ν . This controller yields $\ddot{y}_s = \nu$ and the following linearized output dynamics with linear system coordinates $\xi = (y_s^T, \dot{y}_s^T)^T$,

$$\dot{\xi} = \underbrace{\begin{bmatrix} 0 & I \\ I & 0 \end{bmatrix}}_F \xi + \underbrace{\begin{bmatrix} 0 \\ I \end{bmatrix}}_G \nu.$$

We solve the continuous time algebraic Riccati equation,

$$F^T P + P F - P G G^T P + Q = 0,$$

for this linear system with user-selected weighting matrix $Q = Q^T > 0$, for $P = P^T > 0$ to construct a RES-CLF per the methods of [8]:

$$\bar{V}_\varepsilon^s(\xi) = \xi^T \begin{bmatrix} \frac{1}{\varepsilon} I & 0 \\ 0 & I \end{bmatrix} P \begin{bmatrix} \frac{1}{\varepsilon} I & 0 \\ 0 & I \end{bmatrix} \xi =: \xi^T P^\varepsilon \xi.$$

Taking the derivative gives the convergence constraint:

$$\dot{\bar{V}}_\varepsilon^s(\xi, \nu) = L_F \bar{V}_\varepsilon^s(\xi) + L_G \bar{V}_\varepsilon^s(\xi) \nu \leq -\frac{1}{\varepsilon} \frac{\lambda_{\min}(Q)}{\lambda_{\max}(P)} \bar{V}_\varepsilon^s(\xi),$$

with Lie derivatives along the linearized output dynamics as,

$$L_F \bar{V}_\varepsilon^s(\xi) = \xi^T (F^T P_\varepsilon + P_\varepsilon F) \xi,$$

$$L_G \bar{V}_\varepsilon^s(\xi) = 2 \xi^T P_\varepsilon G.$$

ID-CLF-QP+ F_f . We can write this RES-CLF and its derivative in terms of x and \mathcal{X} to use in the ID-CLF-QP since ξ depends on x_s through $y_s(x_s)$ and $\dot{y}_s(x_s)$ and the relationship in (20) shows ν depends on \mathcal{X} :

$$\nu = L_{\bar{f}^s}^2 y_s(\mathcal{X}) + L_{\bar{g}^s} L_{\bar{f}^s} y_s(\mathcal{X}) u_s(\mathcal{X}). \quad (14)$$

We hence obtain the subsystem RES-CLF (10) with $\bar{c}_1^s = \lambda_{\min}(P)$, $\bar{c}_2^s = \lambda_{\max}(P)$, and $\bar{c}_3^s = \frac{\lambda_{\min}(Q)}{\lambda_{\max}(P)}$.

To avoid the matrix inversions required by (14), we use the facts that $\nu = \ddot{y}_s$ and the output $y_s(x_s)$ is a positional constraint, i.e. $y_s(\bar{q})$, to write the \ddot{y}_s in terms of the robotic subsystem's configuration coordinates \bar{q} :

$$\ddot{y}_s = \underbrace{\frac{\partial}{\partial \bar{q}} \left(\frac{\partial \bar{y}_s}{\partial \bar{q}} \dot{\bar{q}} \right)}_{\dot{J}_y(\bar{q}, \dot{\bar{q}})} \dot{\bar{q}} + \underbrace{\frac{\partial y_s}{\partial \bar{q}}}_{J_y(\bar{q})} \ddot{\bar{q}}. \quad (15)$$

This formulation equates to (14), as shown by [10].

To prescribe a PD controller to \ddot{y} with a control input u_s close to (13), we define $\nu = K_p y^s(x_s) + K_d \dot{y}^s(x_s) := \nu_{pd}$

and minimize the difference between ν_{pd} and (15) in the QP cost. We also include the holonomic constraints in the cost as soft constraints since these are difficult to satisfy precisely on hardware. With decision variables $\Upsilon = (\ddot{q}^T, u_s^T, \bar{\lambda}_h^T, \delta)^T \in \mathbb{R}^{\eta_v}$, with $\eta_v = \bar{\eta} + m_s + \bar{\eta}_h + 1$, and using the terms,

$$J_c(\bar{q}) = \begin{bmatrix} J_y(\bar{q}) \\ \bar{J}_h(\bar{q}) \end{bmatrix}, \quad \dot{J}_c(\bar{q}, \dot{\bar{q}}) = \begin{bmatrix} \dot{J}_y(\bar{q}, \dot{\bar{q}}) \\ \dot{\bar{J}}_h(\bar{q}, \dot{\bar{q}}) \end{bmatrix},$$

we formulate our **ID-CLF-QP+ F_f** :

$$\begin{aligned} \Upsilon^* = \underset{\Upsilon \in \mathbb{R}^{\eta_v}}{\text{argmin}} & \left\| \dot{J}_c(\bar{q}, \dot{\bar{q}})\dot{\bar{q}} + J_c(\bar{q})\ddot{\bar{q}} - \mu^{\text{pd}} \right\|^2 + \sigma W(\Upsilon) + \rho \delta \\ \text{s.t. } & \bar{D}(\bar{q})\ddot{\bar{q}} + \bar{H}(\bar{q}, \dot{\bar{q}}) = \bar{B}u_s + \bar{J}_h^T(\bar{q})\bar{\lambda}_h + \bar{J}_f^T(\bar{q})F_f \\ & L_F \bar{V}_\varepsilon^s(\mathcal{X}) + L_G \bar{V}_\varepsilon^s(\mathcal{X})(\dot{J}_y \dot{\bar{q}} + J_y \ddot{\bar{q}}) \leq -\frac{\gamma}{\varepsilon} \bar{V}_\varepsilon^s(\mathcal{X}) + \delta \\ & -u_{\max} \leq u_s \leq u_{\max}. \end{aligned} \quad (16)$$

Here $\mu^{\text{pd}} = (\nu_{\text{pd}}^T, 0^T)^T$, the regularization term $W(\Upsilon)$ makes the system well-posed, σ and ρ are user-selected weights, and the relaxation term δ ensures the torque bounds $(-u_{\max}, u_{\max})$ are always feasible. (We leave out the arguments on J_y, \dot{J}_y for notational simplicity.)

B. Controller Realization for Hardware

Since the socket forces F_f were unavailable from current platform sensors, the work of [11] developed a force estimation method to determine $J_f^T(q)F_f$ at each sampling time which we use here. Uniquely in this work for the GRFs, we replace part of $\bar{\lambda}_h$ with pressure sensor measurements.

Residual Dynamics Estimation. We estimate the joint accelerations \ddot{q}^{est} with discrete velocity measurements and time:

$$\ddot{q}_{k-1}^{\text{est}} = \frac{\dot{q}_k - \dot{q}_{k-1}}{t_k - t_{k-1}}.$$

Here k represents the current time step and $k-1$, the previous time step. These estimated accelerations are compared to the expected accelerations of the previous time step $\ddot{q}_{k-1}^{\text{exp}}$ from the dynamics without $J_f^T(q)F_f$:

$$\ddot{q}_{k-1}^{\text{exp}} = \bar{D}(\bar{q}_{k-1})^{-1}(-\bar{H}(\bar{q}_{k-1}, \dot{\bar{q}}_{k-1}) + \bar{B}u_{s,k-1} + \bar{J}_h^T(\bar{q}_{k-1})\bar{\lambda}_{h,k-1}). \quad (17)$$

The difference between these multiplied by the inertia matrix of the previous time step gives the present dynamics not considered in the model, i.e. the residual dynamics, \mathcal{F}_{k-1} :

$$\mathcal{F}_{k-1} = \bar{D}(\bar{q}_{k-1})(\ddot{q}_{k-1}^{\text{est}} - \ddot{q}_{k-1}^{\text{exp}}). \quad (18)$$

To attain a smoother signal we average these residual dynamics for N time steps:

$$\mathcal{F}_{k-1}^{\text{avg}} = \frac{1}{N} \sum_{i=1}^N \mathcal{F}_{k-i}. \quad (19)$$

The average residual dynamics from the previous time step is used in place of $J_f^T(q)F_f$ for the current time step. While this method worked well, improving tracking performance in [11], it did not examine the individual fixed joint forces F_f , but rather the forces projected by $J_f(q)$ into the dynamics.

Socket Force Estimation. For this paper, we only consider the residual dynamics related to the socket forces and obtain

these individual forces through the left pseudo inverse of J_f , i.e. J_f^\dagger , where $J_f^\dagger J_f = I$:

$$F_{f,k-1}^{\text{est}} = J_f^\dagger(\bar{q}_{k-1})\mathcal{F}_{k-1}^{\text{avg}}. \quad (20)$$

Ground Force Determination. While in [11] the holonomic constraint wrench $\bar{\lambda}_h$ gave the GRFs, this rigid-contact model does not hold for a foot contacting a variety of real-world non-rigid terrains. This paper employed an insole pressure sensor to determine the vertical GRF $F_{g,z}$ and pitch ground reaction moment $M_{g,y}$, detailed in Section V. By estimating the fixed joint forces F_f^{est} and determining 2 GRFs, $F_{g,z}$ and $M_{g,y}$, through the pressure sensor measurement, the only remaining unknown force is the horizontal GRF. We solve for the wrench $\lambda_{h,x} \in \mathbb{R}^1$ through the holonomic constraints.

ID-CLF-QP+ $F_f^{\text{est}}+\tilde{F}_g$. The final controller formulation is

$$\begin{aligned} \tilde{\Upsilon}_k^* = \underset{\tilde{\Upsilon}_k \in \mathbb{R}^{\eta_v}}{\text{argmin}} & \left\| \dot{\tilde{J}}_c(\bar{q}, \dot{\bar{q}})\dot{\bar{q}} + \tilde{J}_c(\bar{q})\ddot{\bar{q}} - \mu^{\text{pd}} \right\|^2 + \sigma W(\tilde{\Upsilon}_k) + \rho \delta_k \\ \text{s.t. } & \bar{D}(\bar{q}_k)\ddot{\bar{q}}_k + \bar{H}(\bar{q}_k, \dot{\bar{q}}_k) = \bar{B}u_{s,k} + \bar{J}_h^T(\bar{q}_k)\bar{F}_{g,k} + \bar{J}_f^T(\bar{q}_k)F_{f,k-1}^{\text{avg}} \\ & L_F \bar{V}_\varepsilon^s(\mathcal{X}_k) + L_G \bar{V}_\varepsilon^s(\mathcal{X}_k)(\dot{J}_{y,k}\dot{\bar{q}}_k + J_{y,k}\ddot{\bar{q}}_k) \leq -\frac{\gamma}{\varepsilon} \bar{V}_\varepsilon^s(\mathcal{X}_k) + \delta_k, \\ & -u_{\max} \leq u_{s,k} \leq u_{\max}, \end{aligned} \quad (21)$$

with modified set of decision variables $\tilde{\Upsilon}_k = (\ddot{\bar{q}}_k^T, u_{s,k}^T, \bar{\lambda}_{h,x,k}, \delta_k)^T \in \mathbb{R}^{\eta_v}$ and $\tilde{\eta}_v = \bar{\eta} + m_s + 2$. The decision variable $\bar{\lambda}_{h,x,k}$ is included with the measured GRFs $F_{g,z,k}$ and $M_{g,y,k}$ in $\bar{F}_{g,k} = (\bar{\lambda}_{h,x,k}, F_{g,z,k}, M_{g,y,k})^T$.

Remark. This controller uses 3 holonomic constraints to determine the 1 remaining GRF $\bar{\lambda}_{g,x}$ through the cost. This creates an overdetermined problem to solve for $\bar{\lambda}_{h,x}$ in a balanced way with respect to the 3 constraints instead of strictly enforcing a rigid assumption for the x-direction. One could alternatively determine $\lambda_{h,x}$ through a single constraint. Testing both methods on the prosthesis yielded slightly different tracking but comparative performance.

IV. AMPUTEE-PROSTHESIS MODEL AND GAIT GENERATION

To develop outputs for the human-prosthesis system for the ID-CLF-QP+ $F_f^{\text{est}}+\tilde{F}_g$, we construct a model of the system and use hybrid zero dynamics trajectory generation methods.

Amputee-Prosthesis Model. We model an amputee-prosthesis system as a bipedal robot with 8 links and 12 DOFs, i.e. $\eta = 12$ for (1). The prosthesis subsystem has coordinates $q_s = (\theta_{pk}, \theta_{pa})^T$ for the knee and ankle pitch respectively, making $\eta_s = 2$. The remaining amputee system has coordinates $q_l = (q_B^T, \theta_{lh}, \theta_{lk}, \theta_{la}, \theta_{rh})^T$ defining the floating base at the torso and the left hip, left knee, left ankle, and left hip pitch joints respectively. The fixed joint coordinates q_f define the interface between the amputee's partial thigh and the top of the prosthesis. See Fig. 2. Every non-fixed joint is actuated, giving $m_s = 2$ and $m_r = 4$.

The human subject's height and weight along with human inertia, limb mass, and limb length percentage data from [19], [20] provide the human parameters. We base the prosthesis model parameters on the CAD model of AMPRO3 [21], the transfemoral powered prosthesis used in this work. This full system model gives the dynamics of (1)

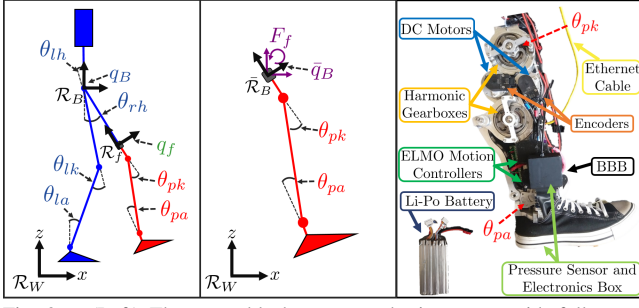


Fig. 2. (Left) The separable human-prosthesis system with full system configuration coordinates. (Middle) The prosthesis equivalent subsystem with subsystem configuration coordinates. (Right) Transference powered prosthesis AMPRO3 with labeled hardware components.

for trajectory generation, for which we omit the ankles since a varying set point PD controller is more comfortable for the user than a prescribed trajectory. The prosthesis equivalent subsystem is constructed with floating based coordinates \bar{q}_B at the socket and (3) gives the dynamics used in (21).

Hybrid Systems and Human-Like Gait Generation. Because bipedal walking contains both discrete and continuous dynamics, we model the amputee-prosthesis system as a hybrid system [22]. Since the amputee-prosthesis system is asymmetrical, we consider two domains of continuous dynamics (1) \mathcal{D}_v with indices $v \in \{\text{ps}, \text{pns}\}$ for prosthesis stance and for prosthesis non-stance, respectively. Each domain has a 3 dimensional holonomic constraint for the respective stance foot ground contact in addition to the fixed joint constraint. Events connect these domains together in a directed cycle, specifically the event of the non-stance foot contacting the ground. The work of [23] explains the impact dynamics occurring at foot-strike.

To design output trajectories for the amputee-prosthesis system that are invariant through impact, we use a hybrid zero dynamics condition [24] in an optimization whose solution must also satisfy the dynamics and feasibility constraints. We design the cost function to minimize the difference between the outputs (the joints) and human walking data obtained through motion capture [25]. The optimization yields parameters for each domain α_v that define Bézier polynomials for the desired trajectories $y_{s,v}^d(\tau(x_s), \alpha_v)$ parameterized by the state-based phase variable $\tau(x_s)$, forward hip position, which goes from 0 to 1 in each domain \mathcal{D}_v [24]. Details given [25]. The resulting trajectories match the human data well and are shown in [11]. Since the optimization gives a prosthesis trajectory that matches human walking data and is stable with the human side emulating the human data, we assume in practice the human will still be able to stabilize itself with the prosthesis following this human-like trajectory. This satisfies the required condition about the human for our main theoretical idea in II to ensure full human-prosthesis system stability for a RES-CLF controlling the prosthesis.

V. GROUND FORCE MEASUREMENT

We obtain real-time force sensing in our model-dependent controller with an insole pressure sensor described here.

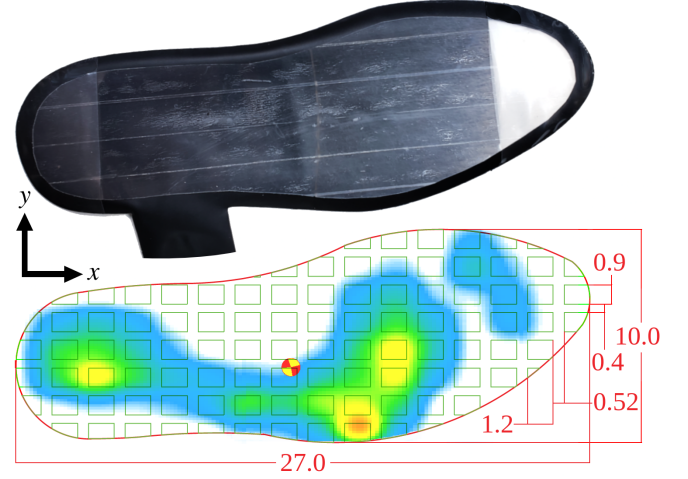


Fig. 3. (Top) Insole pressure sensor. (Bottom) Insole sensor array drawing with dimensions in cm and overlay of colored pressure map from the Tactilus software. The circular marker indicates the CoP estimate.

Pressure Sensor Selection. The pressure sensor used for this study met the restrictive real-time control requirements for our application. Most commercially available insole pressure sensors are designed for recording data for offline gait analysis and are incompatible with our application. First, many insole sensors communicate wirelessly through WiFi or Bluetooth which would introduce a large time-delay, negatively influencing the feedback's effect in real-time control. Second, most companies design pressure sensors with proprietary gait analysis software and the raw data is inaccessible in real-time for custom use. Finally, most wired pressure sensor systems are very expensive, \$10-35k. The sensor for this study is \$2.5-3k and a company-provided API accesses the raw data in real-time over a USB connection.

Pressure Sensor Hardware. The pressure sensor used is a SensorProd Inc. Tactilus Foot Insole Sensor System, High-Performance V Series (SP049), shown in Fig. 3. The sensor is reversible and can be placed in the shoe of either foot. A small electronics box attached to the sensor extends a few inches off of the sensor and can be strapped to the user's or prosthesis' calf. Made of a piezoresistive sensor array, the insole pressure sensor can sense up to 206.8 kPa at 101 separate points per foot. Each sensor element is 0.9 cm \times 1.2 cm \times 0.127 cm in size and has a column pitch of 1.3 cm and a row pitch of 1.72 cm over a total insole size of 10.0 cm \times 27.0 cm, as shown in Fig. 3. The sensor elements are arranged as a 16 \times 8 matrix, although some elements are not present on the insole and give 0 readings. The sensor provides a resolution of $\pm 1 \mu\text{Pa}$ with 12 significant digits at most, along with an accuracy of $\pm 10\%$, repeatability of $\pm 2\%$, hysteresis of $\pm 5\%$, and a non-linearity of $\pm 1.5\%$.

Pressure Sensor Software. We incorporated a Tactilus API, a precompiled C++ Windows Library from SensorProd Inc., into a Windows C++ program which scanned the pressure readings in real time at about 200 Hz. We applied a Gaussian smoothing filter to reduce high differences in pressure readings between adjacent sensor elements potentially due to falsely concentrated readings. This common non-uniform low-pass filter convolves each pressure reading $\mathcal{P}_{i,j}$ of sensor

TABLE I

FORCE MEASUREMENTS WITH FIXED WEIGHTS AND STANDARD ERRORS

Weight (N)	Measured Force (N)
44	29.79±0.04
80.	59.62±0.07
102	94.29±0.11
147	146.26±0.18
169	154.46±0.21
191	187.64±0.37
214	182.54±0.16
236	220.24±0.51

element in row i and column j with the matrix

$$\mathcal{G} = \begin{bmatrix} \frac{1}{16} & \frac{1}{8} & \frac{1}{16} \\ \frac{1}{8} & \frac{1}{4} & \frac{1}{8} \\ \frac{1}{16} & \frac{1}{8} & \frac{1}{16} \end{bmatrix}.$$

Every pressure reading $\mathcal{P}_{i,j}$ is replaced by the filtered reading $\tilde{\mathcal{P}}_{i,j}$, a weighted sum of itself and its surrounding readings:

$$[\tilde{\mathcal{P}}]_{ij} = \sum_{a=i-1}^{i+1} \sum_{b=j-1}^{j+1} \mathcal{G}_{(a-i+2)(b-j+2)} \mathcal{P}_{ab}.$$

At the edges a partial G matrix is used with scaled up weights that sum to 1. To reduce the effect of environmental and systematic high-frequency noise in time, we apply a simple moving average to each $\tilde{\mathcal{P}}_{i,j}$ giving us $\tilde{\mathcal{P}}_{i,j}^{\text{avg}}$.

With $\tilde{\mathcal{P}}_{i,j}^{\text{avg}}$, we

$$F_{g,z} = \sum_{i=1}^{16} \sum_{j=1}^8 w_{ij} \tilde{\mathcal{P}}_{i,j}^{\text{avg}} \Delta x \Delta y, \quad (22)$$

where Δx is the sensor element row pitch, Δy the column pitch, and $w_{i,j}$ a weighting factor based on the approximate percentage of remaining rectangular sensor element. Fig. 3 shows the edge elements are partial rectangles. The numbers 16 and 8 are the total number of rows and columns, respectively. The sensor elements not present on the insole return 0 readings. We obtain the moment by,

$$M_{g,y} = \sum_{i=1}^{16} (x_0 - x_i) \sum_{j=1}^8 w_{ij} \tilde{\mathcal{P}}_{i,j}^{\text{avg}} \Delta x \Delta y, \quad (23)$$

where x_i is the x-position of the sensor and x_0 is the x-position of the selected point of rotation, in this case directly below the center of rotation of the ankle.

Force Measurement Evaluation. We tested the pressure sensor force measurement accuracy by applying fixed weights and recording the measurement. We removed all weight between tests to alleviate the drift affecting the measurements. Table I shows the results, where the force measurements are regularly within $\pm 10\%$ accuracy, especially at higher weights, matching the sensor technical specifications.

Limitations of the sensor include the high propensity to drift, not allowing for an accurate reading of force when a high constant force is applied to the sensor for long periods of time. As much as a 50% change in pressure readings can be attributed to drift. This effect should be minimal in walking where the force is changing throughout each step and being unloaded between strides. Other limitations

include a relatively low maximum pressure on a sensor, 206.8 kPa, which suggests the sensor will be inaccurate when it experiences high concentrated forces. Also an assumption that the surrounding area between sensors have the same pressure as the sensors nearby is made, which may also not be accurate for highly concentrated forces.

VI. HUMAN-PROSTHESIS EXPERIMENTATION

We integrated the pressure sensor into a current powered prosthesis platform to achieve model-based prosthesis control with real-time in-the-loop forcing sensing. The stable human-prosthesis walking results are presented here.

Prosthesis Platform AMPRO3. This study uses the trans-femoral powered prosthesis platform AMPRO3, custom-built and introduced in [21]. Two brushless DC motors (MOOG BN23) with 1 Nm peak torque actuate the knee and ankle pitch joints through their interactions with their respective timing belt connected to each joint's harmonic gear box. This gear reduction system gives a 120:1 mechanical reduction for the knee and 175:1 for the ankle.

The motors are controlled by 2 ELMO motion controllers (Gold Solo Whistle) which receive position and velocity feedback from the 2 incremental encoders, which the motion controllers send to the microprocessor. The microprocessor returns a commanded torque to the motion controllers. The controller algorithms run on the Beaglebone Black Rev C (BBB) microprocessor at 200Hz and are coded in C++ packages with ROS. The coded ID-CLF-QP+ F_f^{rest} + \tilde{F}_g is based on code from [10]. Previously all the computations were done on board the BBB and the prosthesis was a self-contained system powered by a 9-cell 4400 mAh Li-Po battery (Thunder Power RC). For this paper, a pressure sensor was integrated into the system and required a wired connection to a PC for use of the pressure sensor's Windows-specific software. The prosthesis was also wired to the Windows PC with an Ethernet cable. Fig. 2 shows AMPRO3 with the aforementioned components labeled.

Sensor Integration. The insole sensor is physically integrated into the prosthetic system through placement over the insole of a Converse All-Star Men's Size 9 Wide shoe which is worn by the foot of AMPRO3. This shoe has a flat, stiff sole, allowing the sensor to lie flat and be more sensitive to pressure changes during a step. The sensor connects to a Windows PC through USB, and sends force and moment measurements to the BBB through UDP over Ethernet. There is a 5 ms time delay between when the sensor pressure is read and the BBB receives the data caused largely by the time it takes the Windows program to receive all the data from the sensor. Fig. 4 shows a software flow diagram.

Hardware Results. A 1.7 m, 62 kg non-amputee human subject tested the prosthesis device with an iWalk adapter. The iWalk allows her bent right leg to be strapped to the device for walking as shown in Fig. 1. A foam shoe lift strapped to the bottom of her left leg's shoe evens the length difference between her own left leg and her right leg with the prosthesis. A moving average time window of 2 for

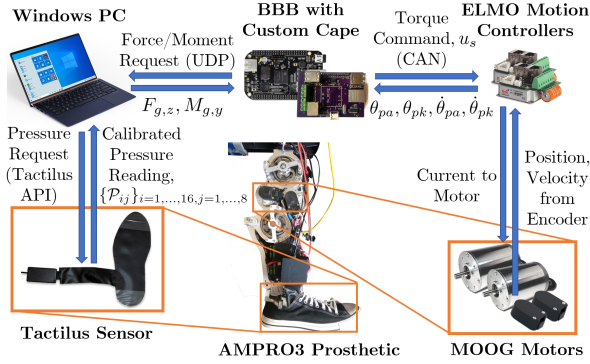


Fig. 4. Hardware and software flow diagram depicting how the pressure sensor communicates and interacts with the prosthesis control scheme.

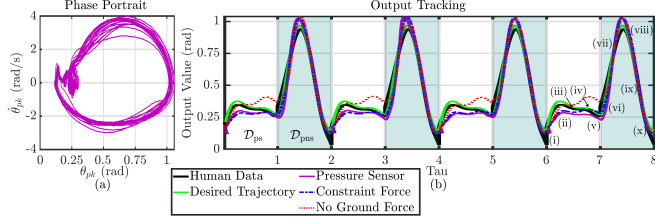


Fig. 5. (a) Phase portrait of the knee joint showing stability of the ID-CLF-QP+ $F_f^{\text{est}} + \tilde{F}_g$ controller (21). (b) Knee output tracking of first four steps of the experiment showing the tracking results of the three stance controllers in D_{PS} (white region) in comparison to each other, the desired trajectory, and the human data. PD controller acting in D_{PNS} (shaded). The numerals correspond to phases of the gait shown in Fig. 1.

the pressure sensor filter and $N = 5$ for the socket force estimator (19) sufficed to provide smooth signals to the controller. We apply the proposed controller to the knee only in stance since this is when the GRFs affect the dynamics. Implementing this model-based controller in swing phase requires an IMU and remains for later work. We applied a PD controller in swing phase for all tests. A PD controller with varying set-point was applied to the prosthesis ankle.

The subject walked with the prosthesis for at least 18 consecutive steps with 3 different controllers in stance on an outdoor level sidewalk. The subject also walked with these controllers on mostly level grass with a small dip. The first controller is the ID-CLF-QP+ $F_f^{\text{est}} + \tilde{F}_g$ (21), the controller of focus in this paper, using the pressure sensor to obtain $F_{g,z}$ (22), $M_{g,y}$ (23). The phase portrait of Fig. 5 a. shows the stability of this main controller. For comparison, we tested a second controller using the original full set of decision variables from (16) in (21) to determine the GRFs with the holonomic constraints instead of the pressure sensor. To test the importance of including all the GRFs in the model, for the third controller we used the same reduced set of decision variables as (21) but did not include the measurements from the pressure sensor such that it only used $\bar{\lambda}_{h,x}$ for the GRFs.

Fig. 5 shows the tracking performance of these three controllers for the first 4 steps cycles of the walking experiments compared to the desired trajectory and the human data used to develop the trajectory. The third controller had the worst tracking performance demonstrating the importance of accounting for all GRFs in this model-based controller. The first and second controllers had slightly different tracking, but similar performance. Their differences again show the GRF model's influence in tracking performance.

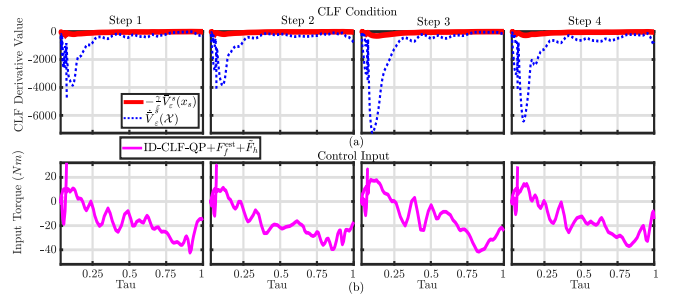


Fig. 6. (a) CLF bound and derivative for first 4 prosthesis stance steps using the ID-CLF-QP+ $F_f^{\text{est}} + \tilde{F}_g$ controller (21), showing the prosthesis remains stable. (b) Respective stance control input for the knee.

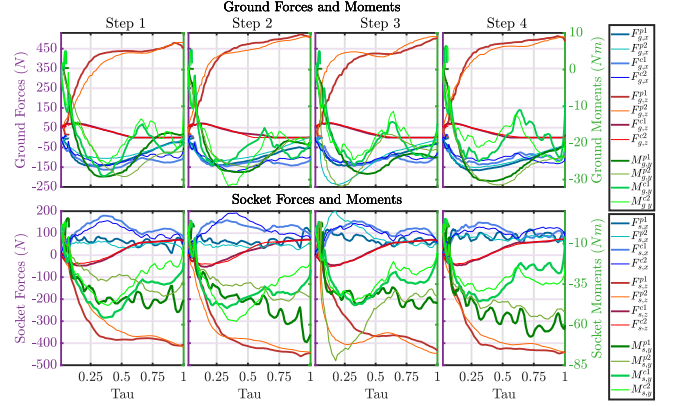


Fig. 7. (Top) Ground reaction forces (left legend) and moments (right legend) determined in the first test on a sidewalk by (21) using a pressure sensor ($\bar{\lambda}_{h,x}^{p1}, F_{g,z}^{p1}, M_{g,y}^{p1}$) and using holonomic constraints ($\bar{\lambda}_{h,x}^{c1}, \bar{\lambda}_{h,z}^{c1}, \bar{\lambda}_{h,y}^{c1}$). The results of the second test on grass are also shown with superscript “p2” for the pressure sensor controller, and “c2” for the constraint controller. (Bottom) The respective estimated socket forces for each of the controllers and tests denoted with subscript “s”.

Fig. 6 a. depicts the CLF derivative remaining below its upper CLF stability bound for the stance phase of the first 4 steps. This shows the advantage of model-dependent control—formal guarantees of stability. Figure 6 b. gives the respective control input for the knee. Note when the CLF derivative is well below its bound, the control input has a relatively low magnitude. This demonstrates another advantage of model-dependent control—when we know the system is very stable, less control input is needed.

Fig. 7 presents the GRFs and socket forces determined for the first 4 prosthesis stance phases by the first two controllers for both sidewalk and grass experiments. The vertical force profile obtained through holonomic constraints remains relatively constant across steps and terrains, which does not reflect the variability that exists between human steps or the different ground responses we expect for softer terrain. The force profiles obtained from the pressure sensor on the other hand vary between steps and between terrain.

Because the constraint controller does not use force sensing, its vertical GRF calculates a maximum of a <75 N force for a 620 N subject. While we do not expect a vertical GRF equal to the subject's weight since the subject's force affects the prosthesis at an angle, we still expect a force of more similar magnitude, like we see with the pressure sensor. These results show how the pressure sensor is able to capture the GRFs better than the holonomic constraints. This first

gives more confidence to our formal guarantees of stability, by having a more accurate model, and second suggests the pressure sensor could aid in control on deformable and uneven terrain encountered in real-life.

(Note: Due to COVID-19 and respective IRB restrictions, this study is limited to one subject on the simple terrains of sidewalks and grass. Future work will examine pressure sensor controller behavior with more subjects on more varied terrain where the rigid contact model is increasingly invalid.)

VII. CONCLUSION AND FUTURE WORK

This work achieved the first experimental realization of a model-dependent prosthesis controller using real-time in-the-loop force measurements to complete the dynamics using an insole pressure sensor resulting in stable human-prosthesis walking. By removing most of the rigid contact assumption and directly measuring the forces, we enable the prosthesis to account for its real-world conditions, increasing the validity of our human-prosthesis stability guarantees. Integration of the insole pressure sensor into the prosthesis platform opens the door to future work accounting for gait stability measures such as CoP in model-dependent prosthesis control methods and gait analysis. Furthermore, this feedback of real-world information provides a means to develop control methods that adapt the prosthesis to its real-time changing terrain. This adaptability would empower amputees to stably walk in a variety of real-world environments such as slopes, uneven terrain, and soft and deformable terrain. These methods could be applied to other lower-limb robotic assistive devices, like exoskeletons, to bring real-world force reaction models into the loop of model-dependent control methods.

Future work will incorporate other plantar pressure data into our control methods and gait analysis to increase stability and prosthesis reactivity. By developing pressure sensor software capable of running on our Linux microprocessor, the BBB, we can reestablish the prosthesis as a self-contained system. Work done for this paper revealed the prosthesis's sensitivity to the value of the x-direction GRF, motivating future use of a sensor capable of detecting lateral force. Incorporating force sensing at the socket interface would further improve the validity of our formal guarantees of stability and increase the prosthesis's ability to account for and react to its real-world conditions. Having access to a CoP measurement enables use of CoP as phase variable [5] and could be used as a guard to determine transitions in multi-domain multi-contact walking [26] for more efficient and human-like walking.

REFERENCES

- [1] E. L. Bukowski, "Atlas of Amputations and Limb Deficiencies: Surgical, Prosthetic, and Rehabilitation Principles, ed 3," *Physical Therapy*, vol. 86, no. 4, pp. 595–596, 04 2006. [Online]. Available: <https://doi.org/10.1093/ptj/86.4.595>
- [2] J. Kulkarni, S. Wright, C. Toole, J. Morris, and R. Hiron, "Falls in patients with lower limb amputations: Prevalence and contributing factors," *Physiotherapy*, vol. 82, no. 2, pp. 130–136, 1996.
- [3] J. Johansson, D. Sherrill, P. Riley, P. Bonato, and H. Herr, "A clinical comparison of variable-damping and mechanically passive prosthetic knee devices," *American journal of physical medicine & rehabilitation / Association of Academic Physiatrists*, vol. 84, pp. 563–75, 09 2005.
- [4] F. Sup, A. Bohara, and M. Goldfarb, "Design and control of a powered transfemoral prosthesis," *The International Journal of Robotics Research*, vol. 27, no. 2, pp. 263–273, 2008, pMID: 19898683.
- [5] R. D. Gregg, T. Lenzi, L. J. Hargrove, and J. W. Sensinger, "Virtual constraint control of a powered prosthetic leg: From simulation to experiments with transfemoral amputees," *IEEE Transactions on Robotics*, vol. 30, no. 6, pp. 1455–1471, Dec 2014.
- [6] C. Kendell, E. Lemaire, N. Dudek, and J. Kofman, "Indicators of dynamic stability in transtibial prosthesis users," *Gait & Posture*, vol. 31, no. 3, pp. 375–379, 2010.
- [7] R. Gehlhar and A. D. Ames, "Separable control lyapunov functions with application to prostheses," *To appear in IEEE Control Systems Letters*, vol. 5, no. 2, pp. 559–564, 2021.
- [8] A. D. Ames, K. Galloway, K. Sreenath, and J. W. Grizzle, "Rapidly exponentially stabilizing control Lyapunov functions and hybrid zero dynamics," *IEEE Transactions on Automatic Control*, vol. 59, no. 4, pp. 876–891, 2014.
- [9] R. Gehlhar, J. Reher, and A. D. Ames, "Control of separable subsystems with application to prostheses," *arXiv preprint arXiv:1909.03102v1*, 2019.
- [10] J. Reher, C. Kann, and A. D. Ames, "An inverse dynamics approach to control lyapunov functions," in *2020 American Control Conference (ACC)*, 2020, pp. 2444–2451.
- [11] R. Gehlhar and A. D. Ames, "Model-dependent prosthesis control with interaction force estimation," in *(To appear in) 2021 IEEE International Conference on Robotics and Automation*, 2021.
- [12] X. Xiong, A. D. Ames, and D. I. Goldman, "A stability region criterion for flat-footed bipedal walking on deformable granular terrain," in *2017 IEEE/RSJ International Conference on Intelligent Robots and Systems (IROS)*. IEEE, 2017, pp. 4552–4559.
- [13] F. Sup, H. A. Varol, J. Mitchell, T. Withrow, and M. Goldfarb, "Design and control of an active electrical knee and ankle prosthesis," in *2008 2nd IEEE RAS EMBS International Conference on Biomedical Robotics and Biomechanics*, 2008, pp. 523–528.
- [14] T. Elery, S. Rezazadeh, C. Nesler, and R. D. Gregg, "Design and validation of a powered knee–ankle prosthesis with high-torque, low-impedance actuators," *IEEE Transactions on Robotics*, vol. 36, no. 6, pp. 1649–1668, 2020.
- [15] M. Schmid, G. Beltrami, D. Zambambieri, and G. Verni, "Centre of pressure displacements in trans-femoral amputees during gait," *Gait & Posture*, vol. 21, no. 3, pp. 255–262, 2005. [Online]. Available: <https://www.sciencedirect.com/science/article/pii/S0966636204000475>
- [16] R. M. Murray, S. S. Sastry, and L. Zexiang, *A Mathematical Introduction to Robotic Manipulation*, 1st ed. Boca Raton, FL, USA: CRC Press, Inc., 1994.
- [17] G. Taga, "A model of the neuro-musculo-skeletal system for human locomotion," *Biol. Cybern.*, vol. 73, no. 2, p. 113–121, Jul. 1995.
- [18] A. Isidori, *Nonlinear Control Systems*. Springer London, 1995.
- [19] S. Plagenhoef, F. G. Evans, and T. Abdelnour, "Anatomical data for analyzing human motion," *Research Quarterly for Exercise and Sport*, vol. 54, no. 2, pp. 169–178, 1983.
- [20] W. Erdmann, "Geometry and inertia of the human body - review of research," *Acta of Bioengineering and Biomechanics*, vol. 1, pp. 23–35, 1999.
- [21] H. Zhao, E. Ambrose, and A. D. Ames, "Preliminary results on energy efficient 3D prosthetic walking with a powered compliant transfemoral prosthesis," in *Robotics and Automation (ICRA)*, 2017 *IEEE International Conference on*. IEEE, 2017, pp. 1140–1147.
- [22] A. D. Ames, "Human-inspired control of bipedal walking robots," *IEEE Transactions on Automatic Control*, vol. 59, no. 5, pp. 1115–1130, 2014.
- [23] J. W. Grizzle, C. Chevallereau, R. W. Sinnet, and A. D. Ames, "Models, feedback control, and open problems of 3d bipedal robotic walking," *Automatica*, vol. 50, no. 8, pp. 1955 – 1988, 2014.
- [24] E. R. Westervelt, J. W. Grizzle, C. Chevallereau, J. H. Choi, and B. Morris, *Feedback control of dynamic bipedal robot locomotion*. CRC press, 2018.
- [25] R. Gehlhar, Y. Chen, and A. D. Ames, "Data-driven characterization of human interaction for model-based control of powered prostheses," in *2020 IEEE/RSJ International Conference on Intelligent Robots and Systems (IROS)*, 2020, pp. 4126–4133.
- [26] H. Zhao, J. Horn, J. Reher, V. Paredes, and A. D. Ames, "Multicontact locomotion on transfemoral prostheses via hybrid system models and optimization-based control," *IEEE Transactions on Automation Science and Engineering*, vol. 13, no. 2, pp. 502–513, April 2016.